Interest of multiple scattering consideration to improve the simulation of ultrasonic FMC/TFM techniques applied to porosity cluster imaging.

Julien VASSEUR[1], Nicolas LEYMARIE[2], Vincent DORVAL[2],
Benoît DUPONT[3], Dmytro VASIUKOV[1], Salim CHAKI[1]
[1] Univ. Lille, IMT Nord Europe, Douai, France
[2] Université Paris-Saclay, CEA, LIST, F-91120, Palaiseau, France
[3] CETIM, Senlis, France

Abstract:

Ultrasonic imaging techniques using Total Focusing Method (TFM) are very useful for positioning and sizing defects with accuracy. However, concerning porosity clusters, the response may be affected by multiple scattering phenomena. This paper deals with a 2D representation of sets of side-drilled holes that are easy to create with reproducible properties (position and size) for experimental tests. The application of a multiple scattering model to this problem is proposed. Several TFM simulations have been performed and compared to experimental results. TFM images simulated with multiple interactions are similar to the experimental images.

Keywords: porosity cluster, ultrasonic testing, multiple scattering model, FMC/TFM imaging, simulation, experimental comparisons

Highlights:

- Simulation of the inter-element response integrating a multiple scattering model with an approximation of scattering coefficients using the far-field assumption;
- Integration of the computational kernel into the NDT CIVA simulation platform developed by French CEA and its partners;
- Comparison of simulated FMC/TFM reconstructions with experimental measurements for several porosity cluster configurations.

1. Introduction

1.1. Global context

The global context of these works is based on the following two observations:

- The lifetime of a structure submitted to fatigue loading is highly affected by the presence of a porosity cluster and the prediction of this lifetime depends on the knowledge of the characteristics of this cluster;
- The detection and characterization of porosity clusters is a complex issue in NDT field.

Concerning the NDT issue, radiographic testing is often applied to detect such defects in casting or forging parts and for weld inspection. It is limited by the characteristics of the part (dimensions,

[1] Contact author: nicolas.leymarie@cea.fr

material) and sometimes not applicable due to the accessibility. The use of ionising radiations is also an issue for environment and safety reasons. It is then possible to apply ultrasonic testing, but this type of defect is not always easy to detect due to the low diffusion of the wave resulting from the small size of the elementary pores and its absorption by the group of pores. For example, in conventional UT, when defects are usually detected by the apparition of an echo, standards introduce the detection of such defects by the analysis of the attenuation or loss of the backwall echo. The consequence for the fatigue issue is that conventional NDT is only able to give a global envelop of the porosity cluster. The fatigue lifetime prediction is then highly affected by the low level of characterization of the defect. Moreover, at the beginning of our works, the influence of the individual characteristics of a porosity cluster (elementary and global size, distribution, etc.) was unknown.

Considering our overall research project, in order to classify the characteristics of the cluster regarding the fatigue lifetime, it was necessary to study experimentally each parameter and manufacture specific samples. Due to the difficulty to manage all the parameters of real porosities clusters which are 3D-defects, it was, as a first step, reduced to a 2D-problem. Clusters of parallel cylindrical holes were chosen to represent porosities, since all their parameters are manageable. Finally, the use of advanced ultrasonic imaging looked to be an interesting solution to overcome the limitations of conventional NDT and determine the characteristic of a porosity cluster.

1.2. Objectives

This paper aims at presenting our works concerning the improvement of detection and characterization of porosity clusters in isotropic materials by using Total Focusing Method. A better understanding of ultrasound interactions with such defects is needed to improve image reconstruction. At the end of the project, this improved and advanced imaging will allow to measure as precisely as possible geometrical characteristics of the porosity clusters (elementary and global size, distribution etc.) to be considered in fatigue lifetime prediction (experimental and numerical results are published in [1]).

This article focuses on the advanced imaging NDT method applied for porosity clusters detection and characterisation. For this purpose, we use the multiple scattering theory for porosity cluster detection and reconstruction by ultrasonic testing simulation, and compare its realism with other reconstructions adopting weaker hypotheses. Real porosity clusters have complex 3D geometrical shapes that are difficult to control and reproduce in the laboratory sample. Therefore, the study was reduced to a 2D problem. As introduced in the global context and for fatigue considerations, clusters of porosities were represented by parallel cylindrical holes. The idea is to solve a 2D problem and put into practice the theoretical developments about multiple scattering that will be shown on schematic clusters of drilled samples. A better comprehension of the wave propagation phenomena in the cluster is necessary to set up the inspection and analyse the obtained images to determine the different characteristics of the cluster (elementary and global size, distribution etc.).

After a brief bibliographic review, we explain our protocol and present the use cases. Then, we summarize the multiple scattering theory. It was implemented in a modified CIVA program and can be applied to any cylinders' configuration (number, diameters and positions). Third, we carry out FMC/TFM reconstructions based on three sets of simulated data: one is the current CIVA simulation including geometrical shadowing effects, another is a modified CIVA simulation with strict single scattering, a third one is another modified CIVA simulation that relies on the proposed multiple scattering model. All these simulation results are then compared with the one obtained

experimentally. We finally show that the accuracy of our multiple scattering method should permit a more efficient detection and characterization of the cluster of cylinders.

1.3. Bibliography

In terms of normalization, there is no standardized method to detect and characterize multiple interacting closely spaced defects. However, the theory of multiple scattering waves is a known problem since at least the ‘40s [2]. The developments began with simple geometric forms, particularly spheres [3–5] and cylinders [6]. The phenomenon was also studied for more complex geometries for example cylinders with arbitrary cross section [7]. The case of several parallel cylinders is particularly studied, for example in [8–10]. This represents indeed important developments which were abundantly used for the study of composites [11,12]. Thus, when the spatial configuration of scatterers show a periodicity, some authors propose for example to calculate a modified Green function [13] to compute the transmission and reflection coefficients of an infinite array of cylinders with any cross section. The multiple scattering model used in this type of paper is based on a scattering matrix, developed in the ‘70s [14]. The theory of multiple scattering can also be used for other defect distributions, like lines of equally spaced obstacles [15], or very close defects not equally spaced [16] or random distribution [17]. The simple diffusion by a unique defect of elastic/fluid/rigid inclusion or a cavity of any shape in a solid matrix is known since at least the ‘70s [18]. But when multiple defects exist (two defects at least), interactions between them occur and mode conversions can appear in solid media as well as some resonance phenomena around the defects [19]. Lastly, we can mention the method of ray tracing to treat the problem of multiple scattering [20].

Following these reminders of bibliography, we precise that to our knowledge, our contribution is first application of multiple diffusion theory for the analytical simulation of imaging an ultrasonic control.

2. Presentation of the protocol

2.1. Presentation of the samples

As mentioned earlier, it was necessary to simplify the study to a 2D problem. Porosities clusters were assimilated to sets of cylindrical Side Drilled Holes (SDHs), which are arranged in a plate tensile specimen with a rectangular cross-section (see Fig. 1). These specimens allow performing ultrasonic inspection and fatigue tests, which consist of oscillating tensile stress at a fixed level of load in order to obtain the corresponding lifetime.

This type of defect is easier to implement and reproduce than real porosities. This problem is invariant along the width.

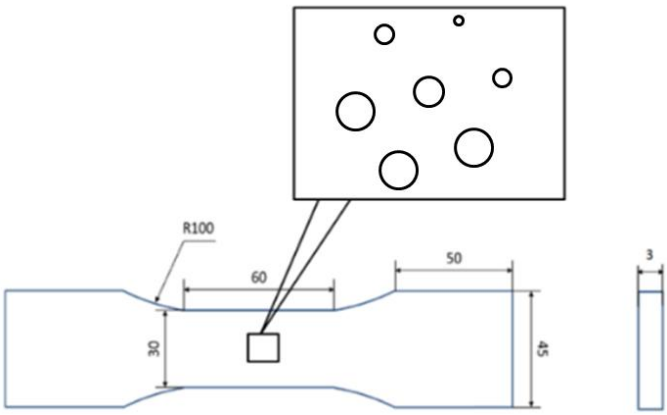

Fig. 1. Illustration of the sample with a considered set of SDHs.

Samples are in aluminium 7075-T6 with isotropic elastic properties. In the following, the wave velocities are chosen such as $c_L = 6.26\, mm/\mu s$ and $c_T = 3.16\, mm/\mu s$ for the longitudinal and transversal waves respectively.

2.2. Characteristics of the SDHs batches

In these works, different characteristics of a porosities cluster were considered. As already mentioned, we choose to assimilate porosity clusters to SDHs with different levels of realism based on geometrical characteristics of the cluster: the elementary size of the pores within the cluster, the number of pores, the different sizes of the pores within the cluster. The adopted choice of SDHs to represent porosities clusters is the result of a compromise between the feasibility of our parametric study (the possibility to manage all geometrical parameters of the cluster) and the realism of the defects.

The SDHs are arranged in hexagons rotated by 15° to avoid alignments effects (for fatigue and inspection considerations), which could be not representative of porosity defect. All these sets of SDHs are circumscribed in a circle of 2 mm diameter. A sample with a unique SDH of 2 mm diameter was called “envelop case” and was used for calibration of the ultrasonic testing.

Ultrasonic inspections were made on these different batches. In this paper, for concision, we only present prevision and experimental results obtained for two sets of seven SDHs (see Fig. 2).

Table 1. Description of the batches.

Batch 0: **Reference** Batch	1 SDH of 2 mm diameter
Batch 1: **Standard**	7 SDH of 300 µm diameter spaced by 1 mm (in a 2 mm diameter circle).
Batch 2: **Gradient** (different sizes)	7 SDH of different diameters spaced by 1 mm (in a 2 mm diameter circle). 1 hole of 150 µm 2 holes of 200 µm 1 hole of 300 µm 3 holes of 400 µm

An illustration of the two configurations is shown in Fig. 2 below with the enumeration of the holes adopted in the following. Batch 2 (gradient) has a positive configuration (incident wave coming from the top, so going through holes from the smallest to the largest ones) and a negative one (incident wave coming from the bottom, so going through holes from the largest to the smallest).

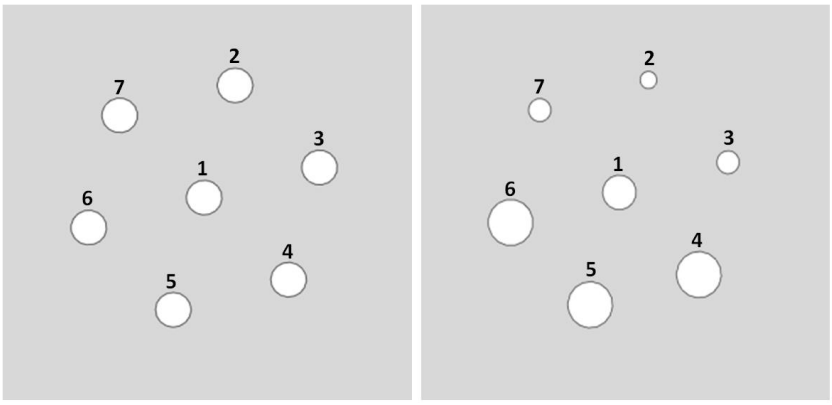

Fig. 2. Illustration of the 2 configurations described, batch 1 on the left, batch 2 on the right.

2.3. Parameters of the ultrasonic inspection and simulations

The device used is a Multi X system (M2M), with a capacity of 128 parallel channels. We use a 64-element-array-probe of 3 mm wide, which elementary size is 0.1 mm and pitch is 0.12 mm with a

central frequency of 15 MHz (see Fig. 3). We apply a band-pass filter from 10 MHz to 30 MHz to the recorded signals.

Fig. 3. Photograph of the material for ultrasonic control which was used

The imaging technique chosen is the FMC/TFM [21] (Full Matrix Capture / Total Focusing Method), considering signal envelopes for amplitude estimation [22]. The reconstruction zone has a dimension of 3.2x3.2 mm and 50 points per millimetre in both directions. It is set centred on the defects zone, which is itself centred on each sample.

To perform the experimental acquisitions, the samples and the probe are fixed in a 3D printed support allowing reproducible measurements and ensuring correct positioning of the probe (as shown in Fig. 4). Experimental reconstructions were made on each set of defects with incident wavefronts coming from the top of the cluster. For gradient batch which is not symmetrical, tests were also made from the bottom edge of the samples.

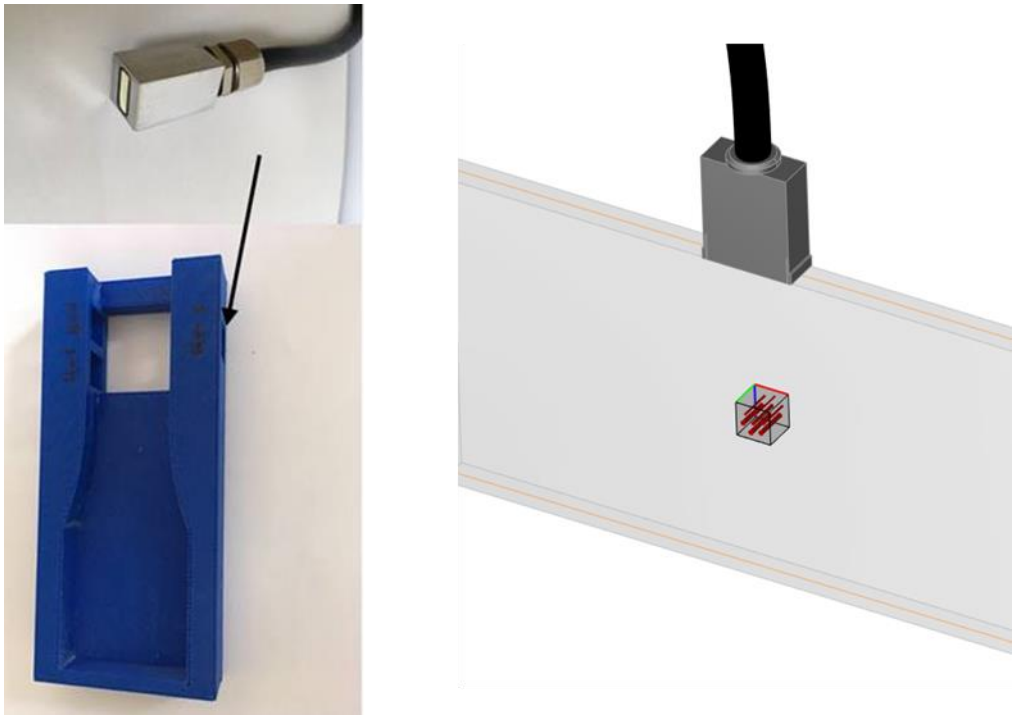

Fig. 4. 3D printed support to hold the sample and phased array above the SDHs clusters.

To begin with this work, we introduce first the formalism of single and multiple scattering aiming at the simulation of a FMC/TFM test on this type of defects.

3. Model description for TFM imaging simulations

3.1. General principle used for echo-response computation

The simulated data that will be presented in this paper were obtained using a modified version of the CIVA software. The modifications allow comparing three ways to compute the echoes from a cluster of cylinders. All of them rely on the ray-based simulation described in [23]. Its general principle is to compute incident and observed ultrasonic fields using a paraxial ray technique [24], and then to compute echoes by summing the interactions of each pairs of incident and observed rays with the scatterer. The expression of the resulting echoes can be summarized as follows:

$$S_{echo} = S_{input} \sum_{s} \sum_{i_{Em}} \sum_{j_{Re}} U_{i_{Em}}^{\mathbf{x}_s} U_{j_{Re}}^{\mathbf{x}_s} A_s \left(\mathbf{d}_{i_{Em}}^{\mathbf{x}_s}, \mathbf{p}_{i_{Em}}^{\mathbf{x}_s}, \mathbf{d}_{j_{Re}}^{\mathbf{x}_s}, \mathbf{p}_{j_{Re}}^{\mathbf{x}_s} \right) \quad (1)$$

Frequency domain notations are used here for brevity, even though in practice a large part of the computation is implemented in the time domain. S_{echo} is the computed echo signal and S_{input} corresponds to the input signal which integrates the sensitivity of our acquisition system via a calibration procedure. The three summations are over scatterers s, and over the emitted and received rays indices i_{Em} and j_{Re}. $\mathbf{x}_s$ is the location of the current scatterer. U is the amplitude of the ultrasonic field corresponding to a ray contribution, $\mathbf{d}$ and $\mathbf{p}$ are its direction and polarization vectors respectively. A_s is the interaction coefficient of the scatterer. This equation is sufficient to describe the computations presented here, but a more general version would include a summation over different modes. For array probes in FMC mode such as the ones considered here, an echo signal is computed for each pair of emitting and receiving elements in order to obtain the entire inter-element signal matrix.

Three types of computations results are presented, corresponding to three ways to apply equation (1). The first one is a strict single scattering approach where the rays and their amplitudes at a given scatterer are entirely independent of the others. The rays can therefore cross other scatterers and no geometrical shadowing is taken into account. The second type of computational result adds this geometrical shadowing: for a given scatterer, only the rays that did not cross another scatterers will be taken into account. It is the approach applied in the commercial version of CIVA. These two computations both use interaction coefficients A_s deduced from single scattering expressions for each SDH. In the third approach, the cluster of SDHs is treated as a global set of scatterers taking into account multiple wave interactions phenomena. The incident and received fields are computed at the barycentre of the cluster and do not account for the presence of the SDHs. The response of the cluster is given by multiple scattering coefficients that account for all types of interactions between the SDHs, including shadowing. For single and multiple scattering coefficients, each ray is assumed to locally behave like a plane wave. That assumption requires the dimensions of the defect cluster to be small compared to its distance to the probe, which is the case for our application. Let us summarise the way to determine the different formulations used to calculate these diffusion coefficients.

3.2. Diffraction models proposed: from single to multiple diffraction

Considering an incident longitudinal (respectively transversal) plane wave in an isotropic elastic media with an incident angle θ_0 at a point P located by (r, θ) in the cylindrical coordinates, we can define the incident displacement potential ϕ_{inc} (resp. ψ_{inc}) as follows [25]:

$$\begin{cases} \phi_{inc}(P,\theta_0) = \phi_0.e^{i\omega t}.\sum_{n=-\infty}^{+\infty} \alpha_n.J_n(k_L.r).e^{in\theta} \ (for\ a\ L\ incidence) \\ \psi_{inc}(P,\theta_0) = \psi_0.e^{i\omega t}.\sum_{n=-\infty}^{+\infty} \alpha_n.J_n(k_T.r).e^{in\theta} \ (for\ a\ T\ incidence) \end{cases} \quad (2)$$

where J_n is the Bessel function of order n, $\alpha_n = i^n.e^{-in\theta_0}$ and $k_{X\,=\,L\,or\,T}$ the wavenumber of the considered wave. In the following, note that *L* and *T* indicate respectively longitudinal and transversal (shear) waves contributions. Considering a unitary incident wave, i.e. ϕ_0 or $\psi_0 = 1$, and implicit time dependency, i.e. omitting $e^{i\omega t}$, the scattered potential displacement must respect the Sommerfeld conditions and must therefore be expressed as an infinite sum of first-order Hankel functions such as:

$$\begin{cases} \phi_S(P,\theta_0) = \sum_{n=-\infty}^{+\infty} \alpha_n.T_n^{(\mathrm{XL})}.H_n^{(1)}(k_L.r).e^{in\theta} \ \text{(for L wave scattering)} \\ \psi_S(P,\theta_0) = \sum_{n=-\infty}^{+\infty} \alpha_n.T_n^{(\mathrm{XT})}.H_n^{(1)}(k_T.r).e^{in\theta} \ \text{(for T wave scattering)} \end{cases} \quad (3)$$

where $T_n^{(\mathrm{XY})}$ is the single scattering coefficient of the cylindrical wave of n^{th} order of incident polarity X = L or T scattered in the polarity Y = L or T. In practice this infinite summation over the orders is limited depending on the dimensions of the cavity and the frequency range studied. In the following, we will note N_{max} the maximum order for which the $T_n^{(\mathrm{XY})}$ coefficients are considered negligible with $n \in [-N_{max}, N_{max}]$.

The principle of multiple scattering consists in taking into account the contribution of a diffracting object's object not only for the primary field from the radiating source, but also for the diffraction contributions of the other diffracting objects subjected to this same source. In this sense, it differs from the single scattering model where only the primary source interaction is taken into account and ignores the contributions of other neighbouring objects as depicted in Fig. 5. For the case of multiple parallel cylinders, the theoretical formalism of the multiple scattering method is established for several decades with well-known reference papers [6,26] for this kind of configuration already mentioned below.

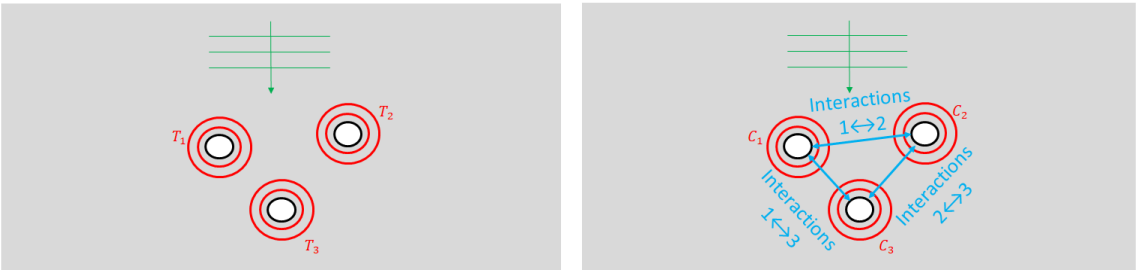

Fig. 5. Schematic representation of the difference between single (on the left) and multiple scattering (on the right) taking into account interactions

The method aims at setting a system to find the multiple scattering coefficients $C_n^{s_i(\mathrm{XY})}$ which are the coefficient of multiple diffractions associated with the wave of n^{th} order of the i^{th} defect for an incident polarity *X* and diffracted polarity *Y*. In this work, we have used the same formalism defined in [27] which gives the following matrix system to solve the problem of the multiple diffraction $\forall n \in [-N_{max}, N_{max}]$ for *X = L or T*:

$$\begin{cases} C_n^{s_i(\mathrm{XL})} - T_n^{s_i(\mathrm{LL})}.\sum_{s_j\neq s_i}\sum_{m=-N_{max}}^{N_{max}} G_{mn}^{s_j s_i(\mathrm{L})}.C_m^{s_j(\mathrm{XL})} - T_n^{s_i(\mathrm{TL})}.\sum_{s_j\neq s_i}\sum_{m=-N_{max}}^{N_{max}} G_{mn}^{s_j s_i(\mathrm{T})}.C_m^{s_j(XT)} = T_n^{s_i(\mathrm{XL})}.\alpha_n^{s_i} \\ C_n^{s_i(\mathrm{XT})} - T_n^{s_i(\mathrm{LT})}.\sum_{s_j\neq s_i}\sum_{m=-N_{max}}^{N_{max}} G_{mn}^{s_j s_i(\mathrm{L})}.C_m^{s_j(\mathrm{XL})} - T_n^{s_i(\mathrm{TT})}.\sum_{s_j\neq s_i}\sum_{m=-N_{max}}^{N_{max}} G_{mn}^{s_j s_i(\mathrm{T})}.C_m^{s_j(\mathrm{XT})} = T_n^{s_i(\mathrm{XT})}.\alpha_n^{s_i} \end{cases} \quad (4)$$

Coefficients $G_{mn}^{s_j s_i(\mathrm{Y})}$ are Graf operators allowing expressing the Y waves scattered by the j^{th} scatterer as incident waves on the i^{th} one, and unknowns $C_n^{s_i(XY)}$ take into account phase shift as already introduced in Eq. (3).

The first (resp. second) equation shall be seen as the synthesis of the incident field and scattered field of L polarity (resp. of T polarity) for the i^{th} defect and for the waves of n^{th} order. Note that Eq. (4) is reduced to a finite problem by replacing the theoretical infinite sums with sums from $-N_{max}$ to N_{max} where N_{max} was chosen to be large enough for the results to converge, while avoiding too large values that tend to induce ill-conditioned matrix problems and long calculation time. Its value depended on the frequency and was at most 14 over the bandwidth of interest.

Taking the convention for the total displacement field such as $\vec{u} = -\overrightarrow{grad}\,\phi + \overrightarrow{rot}\vec{\psi}$, the scattered field of displacement can be expressed with respect to these potential quantities:

$$\begin{cases} \phi_s^{\mathrm{X}}(P,\theta_0) = \sum_{s_i}\sum_{n=-N_{max}}^{N_{max}} C_n^{s_i(\mathrm{XL})}.H_n^{(1)}\left(k_L.r_{s_i}\right).e^{in\theta_{s_i}} \\ \psi_s^{\mathrm{X}}(P,\theta_0) = \sum_{s_i}\sum_{n=-N_{max}}^{N_{max}} C_n^{s_i(\mathrm{XT})}.H_n^{(1)}\left(k_T.r_{s_i}\right).e^{in\theta_{s_i}} \end{cases} \quad (5)$$

Considering free boundary conditions on scatterers, the cancellation of the total stresses (radial and tangential) has been numerically checked on the surface of all cylinders in order to ensure that the estimations of the coefficients $C_n^{s_i}$ are sufficiently correct with respect to the truncation done on orders outside $[-N_{max}, N_{max}]$.

Far-field approximations of these scattered fields can be obtained using the asymptotic forms of Bessel functions for large arguments. This yields expressions such as the following, where far-field scattering coefficients $A_{s_i}^{(\mathrm{XY})}$ appear. For example, in the case of the L-wave scattered mode, we obtain the expression such as:

$$\phi_s^{\mathrm{X}}(P,\theta_0) \approx \sum_{s_i} A_{s_i}^{(\mathrm{XL})}\left(\theta_{s_i}\right)\frac{e^{i.k_L.r_{s_i}}}{\sqrt{r_{s_i}}} \text{ with } A_{s_i}^{(\mathrm{XL})}\left(\theta_{s_i}\right) = \sum_{n=-N_{max}}^{N_{max}} C_n^{s_i(\mathrm{XL})}.\sqrt{\frac{-2i}{\pi k_L}}(-i)^n.e^{in\theta_{s_i}}. \quad (6)$$

Then, for our case where the incident and observation wave type is the longitudinal mode, the $A_{s_i}^{(\mathrm{LL})}$ factors are equivalent to the scattering coefficient A_s of equation (1) and are used to perform multiple-scattering reconstructions. In the following, when comparing with other simplified single scattering models, the same approach is employed by replacing $C_n^{s_i(\mathrm{XL})}$ by $T_n^{s_i(\mathrm{XL})}$ in Eq. (6).

4. Comparison of experimental and simulation results

All the simulated results presented below were performed on the CIVA software platform using existing imaging and analysis tools. As mentioned in the introduction, three types of simulations were performed considering different models in order to simulate the diffraction of our set of SDHs. In the

simplest and fastest case, we will consider the defects independently of each other. We thus place ourselves in a theoretical single scattering hypothesis where the defects do not interact with each other. To denote the results obtained with the single scattering model, we use the acronym SSM. The second model corresponds to the standard model used in the commercial CIVA version. As a reminder, in CIVA, the incident field on a defect is estimated by taking into account other surrounding defects that may be shadowing the target defect. In fact, the ultrasonic field is estimated using a ray model and for any ray intersecting the surface of these neighbouring defects, the contribution is also considered to be zero. In practice, the shadowing effect is taken into account in the amplitude of the incident or observation ray fields (i.e. $U_{i_{Em}}^{\mathbf{x}_S}$ or $U_{j_{Re}}^{\mathbf{x}_S}$ see Eq. (1)) and the scattering coefficient remains the same as for an isolated defect, i.e. $T_n^{(\mathrm{LL})}$ here. The last model using multiple scattering coefficients is much more computationally expensive but should reproduce all the interactions between defects and not only the shadowing effects. Note that in this case, the incident and observation fields are then evaluated without defects. The acronym associated with the model is denoted MSM.

The TFM images obtained from the simulated or experimental inter-element matrix signals are based on the same time-of-flight mapping in the region of interest centred around the defects (as a reminder, 3.2x3.2 mm in dimension).

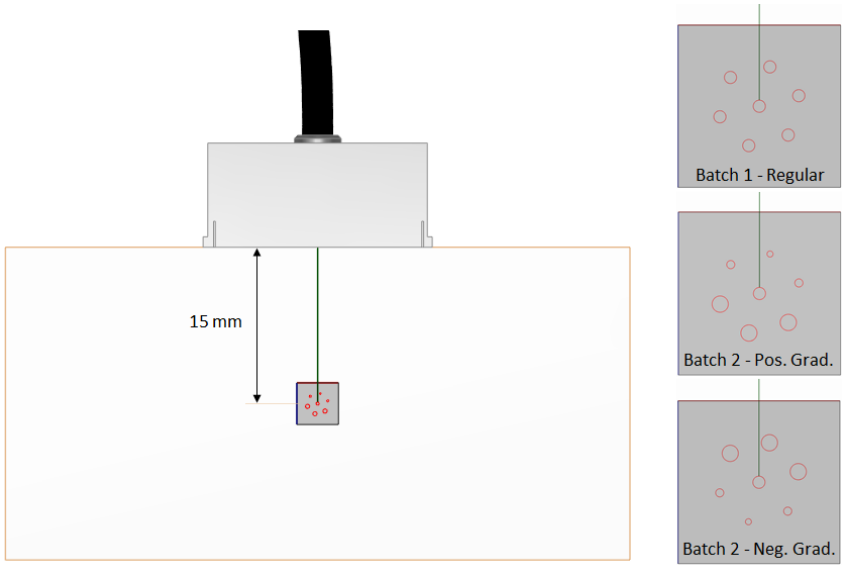

Fig. 6. Illustrations in the CIVA GUI of the defect configurations studied for the comparison of the simulated and experimental TFM images.

As illustrated in Fig. 6, three sets of defects have been studied. In Batch 1 being invariant by a 180°-rotation, only one test of any edge will be presented. Batch 2 shows a positive gradient from the top of the sample (SDHs go bigger during the propagation of the wave) and a negative gradient from the bottom of the sample (SDHs go smaller during the propagation of the wave), thus two tests are needed and presented. The reference in sensitivity (0 dB) is the maximum amplitude from a sample with a 2 mm diameter calibration SDH located at the same depth as the SDHs clusters. The colour scale of all the reconstruction images is linear, with a maximum of 0.5 times the maximum amplitude of the calibration echo corresponding to approximately -6 dB. The numerical values of the maximum amplitudes for all defects are given in tables for each case.

4.1. Batch 1 results

In the following Fig. 7 we show the FMC/TFM reconstructions obtained experimentally on batch 1 and in some different simulation data, with or without interactions or geometrical shadow taken into account.

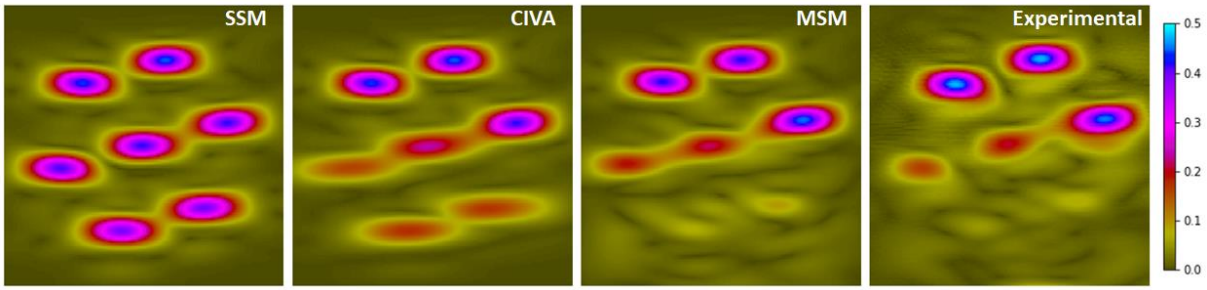

Fig. 7. FMC/TFM reconstruction results of batch 1. From left to right: SSM simulation, standard CIVA simulation, MSM simulation and experimental reconstructions.

We can observe a very good fit between the experimental reconstruction and the one of the modified CIVA program including interactions, particularly concerning the holes #4 and #5 which are less visible than others. Classical CIVA overestimates both. The precise magnitude of each hole is given in Table 2.

Table 2. Comparison of simulated values and experimental amplitudes obtained on holes of batch 1

FMC signal data origin		Relative amplitude of indications (dB)						
		1	2	3	4	5	6	7
Simulations	SSM	-7.6	-7.1	-7.6	-8.1	-8.1	-7.7	-7.3
	CIVA	-12.5	-7.1	-7.6	-15.3	-15.0	-15.9	-7.3
	MSM	-13.3	-7.6	-7.0	-20.6	-23.0	-14.3	-7.6
Experimental		-13.8	-6.5	-6.9	-22.2	-25.5	-15.6	-6.5

Note that in the pure single-scattering simulation, the differences in amplitude between the different defects are primarily due to the ultrasonic beam divergence.

4.2. Batch 2 results

These new FMC/TFM reconstructions were obtained for batch 2 in positive gradient configuration (see Fig. 8) and negative gradient configuration (see Fig. 9). Relative amplitudes of indications are given in Table 3 and Table 4 respectively for positive and negative gradient configuration.

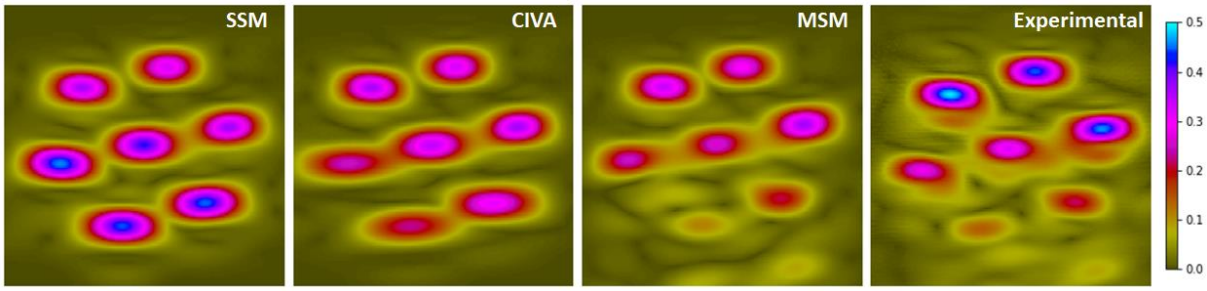

Fig. 8. FMC/TFM reconstruction results of batch 2, positive gradient configuration. From left to right: SSM simulation, standard CIVA simulation, MSM simulation and experimental reconstructions.

Table 3. Comparison of simulated values and experimental amplitudes obtained on holes of batch 2 (positive configuration)

FMC signal data origin		Relative amplitude of indications (dB)						
		1	2	3	4	5	6	7
Simulations	SSM	-7.6	-9.8	-8.8	-7.0	-7.2	-6.8	-8.9
	CIVA	-9.3	-9.8	-8.9	-10.2	-12.8	-11.9	-8.9
	MSM	-11.4	-10.5	-8.8	-13.5	-19.1	-11.9	-9.5
Experimental		-13.8	-10.0	-7.1	-6.8	-13.3	-17.1	-11.0

On the positive gradient configuration, we can see a great realism of the modified CIVA program including interactions, particularly concerning holes #4 and #5. An echo is even visible on the bottom right of experimental and modified CIVA reconstructions clearly due to multiple interactions within the cluster since standard CIVA simulations do not show it.

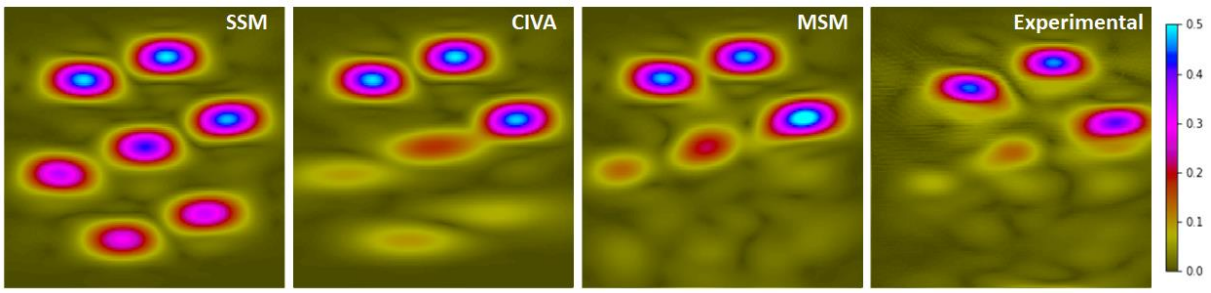

Fig. 9. FMC/TFM reconstruction results of the batch 2, negative gradient configuration. From left to right: SSM simulation, standard CIVA simulation, MSM simulation and experimental reconstructions.

On the negative gradient configuration, we can observe that holes #2 and #7 are not visible according to the multiple scattering simulation. This is confirmed by the experimental reconstruction while standard CIVA simulations do not correctly estimate the response of these two holes.

Table 4. Comparison of simulated values and experimental amplitudes obtained on holes of batch 2 (negative configuration)

FMC signal data origin		Relative amplitude of indications (dB)						
		1	2	3	4	5	6	7
Simulations	SSM	-7.5	-10.7	-9.2	-6.2	-6.1	-6.5	-9.5
	CIVA	-15.2	-20.1	-20.7	-6.3	-6.1	-6.4	-22.7
	MSM	-13.4	-32.0	-17.6	-6.4	-6.4	-5.5	-26.9
Experimental		-13.8	-17.2	-32.4	-23.1	-6.9	-6.7	-7.7

Note that the indication for hole #6 in this batch seems to be slightly overestimated in multiple scattering compared to experimental results and other simulation models. This is probably due to the experimental difficulty of highlighting the interactions between holes #4 and #5, which would effectively induce a strong echo of hole #6. The same remark can be made for hole #3. However, all other echoes are predicted with great realism.

5. Conclusions

A strategy have been presented to guarantee a repeatable protocol for detection of porosities clusters that were assimilated to sets of Side Drilled Holes (SDH) in-plane samples. Thus, the study was reduced to a 2D problem and the geometrical characteristics of the clusters were controlled.

It was shown that while single scattering hypothesis can be a good hypothesis for defects distant from one another, it is not necessarily appropriate for close-packed defects such as porosity clusters. We applied FMC/TFM imaging to such complex configurations of defects, and we compared simulation models with various scattering hypotheses. FMC/TFM reconstructions were simulated by models with several degrees of approximation: pure single scattering, single scattering with shadowing, and multiple scattering. These reconstructions were compared to the equivalent reconstructions obtained experimentally. The results using multiple scattering show a qualitative and quantitative improvement with respect to the measurements. Compared to the other models, it gave more accurate amplitudes for SDH echoes and also correctly predicted the apparition of some virtual echoes arising from multiple interactions.

In the global context of our works that was recalled in the introduction, these results showed a better comprehension of the wave propagation phenomena in the cluster. The improved images obtained should ultimately allow better determination of the different characteristics of the clusters and finally, the prediction of the fatigue life compared to a classical approach.

For the two-dimensional configurations considered here, it can be argued that numerical simulations could be as efficient and more generic than an analytical multiple scattering approach. However, in the case of three-dimensional configurations, an analytical approach may significantly outperform numerical ones. An extension of the multiple scattering simulations presented here to three-dimensional clusters of spherical porosities could therefore be interesting. Additionally, comparisons between measurements and simulations in other frequency ranges exhibiting multiple scattering effects in different ways could be interesting. In fact, at low frequencies, the ultrasound signature of the porosity cluster would potentially be easier to define, in particular by analyzing the coda of the inter-element responses.

CRediT authorship contribution statement

Julien Vasseur: Conceptualization, Methodology, Investigation, Validation, Writing – original draft. **Nicolas Leymarie**: Conceptualization, Methodology, Writing – Review & Editing, Supervision. **Vincent Dorval**: Formal analysis, Software, Validation, Writing – original draft, Visualization. **Benoit Dupont**: Conceptualization, Methodology, Validation, Resources, Writing – Review & Editing, Supervision. **Dmytro Vasiukov:** Conceptualization, Methodology, Writing – Review & Editing. **Salim CHAKI**: Supervision, Conceptualization, Methodology, Writing – Review & Editing.

Declaration of competing interest

The authors declare that they have no known competing financial interests or personal relationships that could have appeared to influence the work reported in this paper.

References

[1] Vasseur J, Lefebvre F, Vasiukov D, Chaki S, Huther I, Marzin M, et al. Methodology of fatigue life assessment on components with porosity clusters. Theor Appl Fract Mech 2020;108:102619. https://doi.org/10.1016/j.tafmec.2020.102619.

[2] Foldy LL. The Multiple Scattering of Waves. I. General Theory of Isotropic Scattering by Randomly Distributed Scatterers. Phys Rev 1945;67:107–19. https://doi.org/10.1103/PhysRev.67.107.

[3] Ying CF, Truell R. Scattering of a Plane Longitudinal Wave by a Spherical Obstacle in an Isotropically Elastic Solid. J Appl Phys 1956;27:1086–97. https://doi.org/10.1063/1.1722545.
[4] Waterman PC, Truell R. Multiple Scattering of Waves. J Math Phys 1961;2:512–37. https://doi.org/10.1063/1.1703737.
[5] Fikioris JG, Waterman PC. Multiple Scattering of Waves. II. ``Hole Corrections'' in the Scalar Case. J Math Phys 1964;5:1413–20. https://doi.org/10.1063/1.1704077.
[6] Twersky V. Multiple Scattering of Radiation by an Arbitrary Configuration of Parallel Cylinders. J Acoust Soc Am 1952;24:42–6. https://doi.org/10.1121/1.1906845.
[7] Varadan VK, Varadan VV, Pao Y. Multiple scattering of elastic waves by cylinders of arbitrary cross section. I. SH waves. J Acoust Soc Am 1978;63:1310–9. https://doi.org/10.1121/1.381883.
[8] Robert S, Conoir J-M, Franklin H, Luppé F. Resonant elastic scattering by a finite number of cylindrical cavities in an elastic matrix. Wave Motion 2004;40:225–39. https://doi.org/10.1016/j.wavemoti.2004.03.003.
[9] Twersky V. On scattering of waves by the infinite grating of circular cylinders. IRE Trans Antennas Propag 1962;10:737–65. https://doi.org/10.1109/TAP.1962.1137940.
[10] Young JW, Bertrand JC. Multiple scattering by two cylinders. J Acoust Soc Am 1975;58:1190–5. https://doi.org/10.1121/1.380792.
[11] Yang R-B, Mal AK. Multiple scattering of elastic waves in a fiber-reinforced composite. J Mech Phys Solids 1994;42:1945–68. https://doi.org/10.1016/0022-5096(94)90020-5.
[12] Lonné S, Lhémery A, Calmon P, Biwa S, Thévenot F. Modeling of Ultrasonic Attenuation in Uni-Directional Fiber Reinforced Composites Combining Multiple-Scattering and Viscoelastic Losses. AIP Conf Proc 2004;700:875–82. https://doi.org/10.1063/1.1711711.
[13] Lynott GM, Andrew V, Abrahams ID, Simon MJ, Parnell WJ, Assier RC. Acoustic scattering from a one-dimensional array; Tail-end asymptotics for efficient evaluation of the quasi-periodic Green's function. Wave Motion 2019;89:232–44. https://doi.org/10.1016/j.wavemoti.2019.01.012.
[14] Pao Y-H, Mow CC. Theory of normal modes and ultrasonic spectral analysis of the scattering of waves in solids. J Acoust Soc Am 1976;59:1046. https://doi.org/10.1121/1.380969.
[15] Twersky V. Multiple scattering of sound by a periodic line of obstacles. J Acoust Soc Am 1973;53:96–112. https://doi.org/10.1121/1.1913334.
[16] Lethuillier S, Conoir JM, Pareige P, Izbicki JL. Resonant acoustic scattering by a finite linear grating of elastic shells. Ultrasonics 2003;41:655–62. https://doi.org/10.1016/j.ultras.2003.07.001.
[17] Varadan VK, Ma Y, Varadan VV. A multiple scattering theory for elastic wave propagation in discrete random media. J Acoust Soc Am 1985;77:375–85. https://doi.org/10.1121/1.391910.
[18] Varatharajulu V, Pao Y. Scattering matrix for elastic waves. I. Theory. J Acoust Soc Am 1976;60:556–66. https://doi.org/10.1121/1.381129.
[19] Flax L, Dragonette LR, Überall H. Theory of elastic resonance excitation by sound scattering. J Acoust Soc Am 1978;63:723–31. https://doi.org/10.1121/1.381780.
[20] Brigante M. On multiple scattering in acoustic media: A deterministic Ray Tracing method for random structures. Ultrasonics 2013;53:652–7. https://doi.org/10.1016/j.ultras.2012.11.013.
[21] Holmes C, Drinkwater BW, Wilcox PD. Post-processing of the full matrix of ultrasonic transmit–receive array data for non-destructive evaluation. NDT E Int 2005;38:701–11. https://doi.org/10.1016/j.ndteint.2005.04.002.
[22] Iakovleva E, Chatillon S, Bredif P, Mahaut S. Multi-mode TFM imaging with artifacts filtering using CIVA UT forwards models. AIP Conf Proc 2014;1581:72–9. https://doi.org/10.1063/1.4864804.
[23] Dorval V, Leymarie N, Chatillon S. Improved semi-analytical simulation of UT inspections using a ray-based decomposition of the incident fields. AIP Conf Proc 2016;1706. https://doi.org/10.1063/1.4940520.
[24] Gengembre N, Lhémery A. Pencil method in elastodynamics: application to ultrasonic field computation. Ultrasonics 2000;38:495–9. https://doi.org/10.1016/S0041-624X(99)00068-2.

[25] Varatharajulu V, Pao Y. Scattering matrix for elastic waves. I. Theory. J Acoust Soc Am 1976;60:556–66. https://doi.org/10.1121/1.381129.
[26] Waterman PC. Matrix theory of elastic wave scattering. 567 J Acoust Soc Am 1976;60:567–80.
[27] Robert S, Conoir J-M, Franklin H, Luppé F. Resonant elastic scattering by a finite number of cylindrical cavities in an elastic matrix. Wave Motion 2004;40:225–39. https://doi.org/10.1016/j.wavemoti.2004.03.003.